



HAL
open science

Pressure-temperature estimates of the lizardite/antigorite transition in high pressure serpentinites.

Stéphane Schwartz, Stéphane Guillot, Bruno Reynard, Romain Lafay, Baptiste Debret, Christian Nicollet, Pierre Lanari, Anne-Line Auzende

► To cite this version:

Stéphane Schwartz, Stéphane Guillot, Bruno Reynard, Romain Lafay, Baptiste Debret, et al.. Pressure-temperature estimates of the lizardite/antigorite transition in high pressure serpentinites.. Lithos, 2012, 178, pp.197-210. 10.1016/j.lithos.2012.11.023 . insu-00854214

HAL Id: insu-00854214

<https://insu.hal.science/insu-00854214>

Submitted on 26 Aug 2013

HAL is a multi-disciplinary open access archive for the deposit and dissemination of scientific research documents, whether they are published or not. The documents may come from teaching and research institutions in France or abroad, or from public or private research centers.

L'archive ouverte pluridisciplinaire **HAL**, est destinée au dépôt et à la diffusion de documents scientifiques de niveau recherche, publiés ou non, émanant des établissements d'enseignement et de recherche français ou étrangers, des laboratoires publics ou privés.

1 **Pressure-temperature estimates of the lizardite/antigorite transition**
2 **in high pressure serpentinites.**

3

4 Stéphane Schwartz¹, Stéphane Guillot¹, Bruno Reynard², Romain Lafay¹, Christian Nicollet³,
5 Baptiste Debret³, Pierre Lanari¹, Anne Line Auzende⁴

6

7

8 1-IsTerre, Université Grenoble 1, CNRS, F-38041 Grenoble, Cedex 9, France.

9 2-Laboratoire de Géologie, Ecole Normale Supérieure de Lyon, CNRS, France, Site Monod,
10 15 parvis René Descartes, Lyon, F-69342, France.

11 3-LMV, Université Blaise Pascal, CNRS, Clermont-Ferrand, France.

12 4-IMPMC, Université Pierre et Marie Curie - Sorbonne Universités, 4 place Jussieu, Tour 23,
13 75252 Paris Cedex 05, France.

14

15

16

17

18 E-mail: stephane.schwartz@ujf-grenoble.fr

19

20 **Abstract**

21 Serpentine minerals in natural samples are dominated by lizardite and antigorite. In
22 spite of numerous petrological experiments, the stability fields of these species remain poorly
23 constrained. This paper presents the petrological observations and the Raman spectroscopy
24 and XRD analyses of natural serpentinites from the Alpine paleo-accretionary wedge.
25 Serpentine varieties are identified from a range of metamorphic pressure and temperature
26 conditions from sub-greenschist ($P < 4$ kbar, $T \sim 200$ - 300°C) to eclogite facies conditions (P
27 > 20 kbar, $T > 460^\circ\text{C}$) along a subduction geothermal gradient. We used the observed mineral
28 assemblage in natural serpentinite along with the T_{max} estimated by Raman spectroscopy of
29 the carbonaceous matter of the associated metasediments to constrain the temperature of the
30 lizardite to antigorite transition at high pressures. We show that below 300°C , lizardite and
31 locally chrysotile are the dominant species in the mesh texture. Between 320 and 390°C ,
32 lizardite is progressively replaced by antigorite at the grain boundaries through dissolution-
33 precipitation processes in the presence of SiO_2 enriched fluids and through a solid-state
34 transition in the cores of the lizardite mesh. Above 390°C , under high-grade blueschist to
35 eclogite facies conditions, antigorite is the sole stable serpentine mineral until the onset of
36 secondary olivine crystallization at 460°C .

37 **Keywords:** Serpentinite; Raman spectroscopy; lizardite/antigorite transition; western Alps

38 1. Introduction

39 Serpentine minerals are phyllosilicates that contain up to 13 wt% water and that form
40 during the hydration of basic to ultrabasic rocks. Hydration commonly takes place in ocean
41 spreading context, thus documenting the chemical exchanges between the oceans and solid
42 Earth (Alt and Shanks, 2003). Serpentinites are also common in blueschist to eclogite facies
43 terranes of oceanic or mantle wedge origin (Hattori and Guillot, 2007). Due to serpentinites'
44 low-variance metamorphic assemblage, it is generally difficult to evaluate the P-T conditions
45 to which they were subjected (e.g., Evans, 2004), but the associated metamorphic rocks
46 permit approximations of the conditions. It is therefore important to accurately and rapidly
47 characterize these common serpentine minerals. Serpentine minerals, which have simplified
48 structure formulae $(\text{Mg, Fe}^{2+})_3 \text{Si}_2\text{O}_5(\text{OH})_4$, are made of superposed 1:1 alternating tetrahedral
49 and octahedral sheets. The different spatial arrangements of these layers result in three main
50 serpentine minerals, i.e., lizardite, chrysotile and antigorite. The sheets form flat layers in
51 lizardite, rolls in chrysotile and curved modulated structures in antigorite (e.g., Wicks and
52 O'Hanley, 1988). Serpentinites in high-grade metamorphic terranes indicate that antigorite is
53 the predominant species (Scambelluri et al., 1995; Trommsdorff et al., 1998; Auzende et al.,
54 2002; 2006; Li et al., 2004; Groppo and Compagnoni, 2007; Padron-Navarta et al., 2008;
55 Guillot et al., 2009). Moreover, experimental studies confirm that antigorite is the stable
56 serpentine mineral under high-pressure conditions (Ulmer and Trommsdorff, 1995; Wunder
57 and Schreyer, 1997; Bromiley and Pawley, 2003; Perrillat et al., 2005; Komabayashi et al.,
58 2005; Reynard and Wunder, 2006; Padron-Navarta et al., 2010). Lizardite and chrysotile are
59 the main varieties that are present in low-grade serpentinites from the oceanic lithosphere and
60 from low-grade metamorphic ophiolites (Evans, 2004; Andréani et al., 2007). However, the
61 transition from low-grade to high-grade serpentine minerals is poorly constrained.
62 Thermodynamic data predict that above 300°C, the antigorite + brucite assemblage is more
63 stable than lizardite, and chrysotile is absent (Evans, 2004). Moreover, the antigorite + brucite
64 assemblage is often observed in natural samples, while the chrysotile + brucite assemblage is
65 particularly abundant in retrogressed serpentinites (Baronnet and Belluso, 2002). Thus, further
66 petrological investigations of natural serpentinite samples, where the P-T conditions are well-
67 constrained, are required to refine the relative stability of each variety of serpentine over a
68 wide range of metamorphic conditions. To definitively identify serpentine varieties,
69 transmission electron microscopy (TEM) is usually required (Mellini et al., 1995; Auzende et
70 al., 2002; Boudier et al., 2010). Indeed, serpentine grains are only a few microns in size and

71 can display various habitus, which makes optical identification inaccurate. Vibrational Raman
72 spectroscopy is also a powerful method for processing large numbers of complex samples,
73 and numerous studies have been devoted to its use in serpentine characterization (Lewis et al.,
74 1996; Bard et al., 1997; Kloprogge et al., 1999; Rinaudo et al., 2003; Auzende et al., 2004;
75 Groppo et al., 2006). In particular, the region of the OH stretching vibrational modes can be
76 conveniently used to discriminate among the different varieties of serpentine (Auzende et al.,
77 2004). The OH stretching modes in the high wavenumber range (approximately 3500 cm^{-1}) of
78 the different serpentines are tentatively described in terms of the curvature of the layers, with
79 potential applications for structural characterization by Raman spectroscopy. Raman
80 spectroscopy permits the characterization of the phases at a micrometer scale of bulk samples
81 or thin sections. To assess the reliability of Raman spectroscopy for identification purposes,
82 we apply it to serpentines in a series of low to high pressure metamorphic serpentinite
83 samples from the western Alps for which TEM characterization have been independently
84 performed (Auzende et al., 2006). The serpentinites are also characterized by XRD in order to
85 decipher the bulk serpentinite mineralogy.

86 **2. Geological setting**

87 Alpine evolution along the Eurasia-Africa boundary was initially dominated by plate
88 divergence, which induced Mesozoic rifting and oceanic opening. Since Cretaceous time, the
89 plate convergence has resulted in subduction and collision (Rosenbaum and Lister, 2005;
90 Dumont et al., 2012). This study focuses on the Piedmont zone of the southwestern Alps (Figs
91 1a and 1b), which is composed of the association of units that originated in the distal
92 European margin and from the nearby oceanic domain (Lemoine et al., 1986) and that were
93 juxtaposed during the subduction and collision in Late Cretaceous to Tertiary times (Tricart,
94 1984). The Piedmont zone includes different levels of the paleo-subduction zone, preserving
95 the low thermal gradient ($5\text{--}8\text{ }^{\circ}\text{C}/\text{km}$) associated with the subduction dynamics; moreover, it
96 is partially overprinted by Alpine metamorphism conditions (Schwartz et al., 2001, 2007,
97 Agard et al., 2002). At the top of the nappe pile, the Chenaillet massif corresponds to an
98 obducted portion of the Tethyan oceanic lithosphere. This unit rests upon the Queyras
99 Schistes lustrés (Fig. 1c), which represents a fossiliferous sedimentary accretionary wedge
100 developed under blueschist facies conditions during the late Cretaceous–early Eocene
101 subduction of the Tethyan Ocean (Schwartz, 2000; Tricart and Schwartz, 2006; Schwartz et
102 al., 2009), as previously indicated by structural observations further to the north in the same
103 Piedmont zone (Agard et al., 2001; Ganne et al., 2005). This domain derived from Mesozoic

104 oceanic sediments that were primarily composed of metamorphic marls, clays, and limestones
105 (calcschists). These sediments were strongly deformed and metamorphosed during alpine
106 subduction, and they outcrop today as foliated and polydeformed calcschists enclosing
107 boudinaged meter- to kilometer-sized Jurassic ophiolites (Tricart and Lemoine, 1986;
108 Lagabrielle and Polino, 1988). The P-T conditions increase towards the east, from low
109 temperature-blueschist facies conditions (LT-blueschist) in western Queyras to the transitional
110 conditions between high-temperature blueschist (HT-blueschist) and eclogite facies in eastern
111 Queyras (Agard et al., 2001; Tricart and Schwartz, 2006; Schwartz et al., 2009). This
112 blueschist domain is structurally above the Monviso eclogitic ophiolite. In this massif, the
113 metasedimentary component is very small (< 20 vol.%) relative to the voluminous oceanic
114 lithosphere (Schwartz et al., 2001). The serpentinite bodies are located along detachments and
115 constitute a large volume of the eastern boundary of the massif (Schwartz et al., 2001,
116 Angiboust et al., 2012). The Monviso ophiolite corresponds to the subduction channel
117 (Guillot et al., 2009).

118 **3. Sampling strategy**

119 The Chenaillet-Queyras-Monviso transect is a unique natural laboratory for observing
120 mineral changes in serpentinite along an increasing metamorphism gradient. However, there
121 are no directly applicable thermal calibrations in serpentinites; therefore, we propose to
122 estimate the thermal conditions by applying the method of Raman spectroscopy of
123 carbonaceous material (RSCM) to the metasediments associated with the serpentinites to
124 obtain the T_{\max} experienced by the serpentinites. A thermal transect is realized, according to
125 25 metasediment samples from the Chenaillet to the Monviso (Fig. 1a, Table 1). These
126 sediments are Cretaceous calcschists derived from foraminifera oozes (Deville et al., 1992).
127 The lithology of each sample is not homogeneous due to the variation in carbonate-clay
128 proportions. Moreover, the carbonate contents result both from biogenic production (pelagic
129 foraminifera) and from detrital input (calciturbidites). The samples are strongly deformed, and
130 the main schistosity is dominated by phengite, quartz, calcite and oxides. Glaucofane and
131 pseudomorphs of lawsonite and zoisite are also present. Along this thermal transect, 7
132 serpentinites have been studied (Fig. 1a). The serpentinite samples were taken from the cores
133 of hecto-metric serpentinite bodies; these bodies were embedded in the metasediments from
134 which the metasediment samples were acquired. These serpentinites escaped alpine
135 deformations and preserved the oceanic mesh textures. Sample ICH2 comes from the
136 ophiolitic Chenaillet massif. This sample records a low degree of metamorphic conditions,

137 with sea-floor metamorphism (Mével et al., 1978) overprinted by sub-greenschist facies
138 conditions ($P < 4$ kbar; $T \sim 200$ - 300°C ; Goffé et al., 2004) related to alpine metamorphism.
139 Sample CR02 comes from the Cristillan massif at the western boundary of the Schistes lutrés
140 complex in the LT-blueschist domain (Fig. 1). Two samples come from the medium-
141 temperature blueschist domain (MT-blueschist) of the Schistes lutrés complex: RQ23 from
142 the Rocca Nera massif and RQ16 from the Eychassier massif. Samples BB01 (Bric Bouchet
143 massif) and RQ01 (Traversette massif) come from the HT-blueschist domain of the Schistes
144 lutrés complex. The final sample, Vi01, comes from the Monviso eclogitic ophiolite.

145 **4. Temperature estimates from Raman spectroscopy of carbonaceous** 146 **material (RSCM)**

147 4.1. Analytical conditions

148 Raman spectroscopy on carbonaceous material (RSCM) is based on the quantitative
149 degree of graphitization of the organic material during regional metamorphic processes. The
150 graphitization phenomenon corresponds to the solid-state transformation of organic matter
151 into carbonaceous material. The structure of carbonaceous matter is not sensitive to the
152 retrograde history related to the exhumation of metamorphic rocks. The progressive
153 graphitization process can be used to estimate the peak temperature (T_{max}) reached by a given
154 sample (Beysac et al., 2002, 2003). The degree of graphitization appears to be independent
155 of the metamorphic pressure, although a minimum pressure is required for the graphitization
156 process to take place (Quirico et al., 2009). This thermometer is based on the quantification of
157 the degree of ordering of the carbonaceous material, using the R2 area ratio between the G,
158 D1 and D2 bands ($R2 = D1/[G+D1+D2]$) extracted from the Raman spectra (Beysac et al.,
159 2002). The R2 ratio is linearly correlated with the T_{max} of the metamorphic cycle ($T_{\text{max}}(^{\circ}\text{C}) =$
160 $-445 \times R2 + 641$). This correlation may be used as a thermometer with an intrinsic error
161 calibration of 50°C due to the petrological data used for calibration and a relative accuracy of
162 approximately 15°C (Beysac et al., 2007).

163 Raman spectroscopy was performed at the ENS-Lyon using a Horiba Jobin-Yvon
164 LabRam HR800 apparatus. The excitation was realized by an argon laser with a wavelength
165 of 514 nm. An OlympusTM BX30 open microscope equipped with a $\times 100$ objective lens was
166 coupled to the spectrometer to focus the laser beam onto an area that was $1 \mu\text{m}$ in diameter.
167 The backscatter of the Raman signal was collected. The acquisition duration was

168 approximately 120 s distributed over two accumulating cycles, with a laser power of
169 approximately 700 μ W at the sample surface. The signal was dispersed using a 1800
170 lines/mm grating. The Raman spectrometer was calibrated with a silicon standard. For each
171 sample, 11 to 13 spectra were recorded (noted 'n' in Table 1). The baseline correction, peak
172 position, and band width were determined using the Peakfit© software.

173 4.2. T_{\max} results

174 From west to east, the Raman spectra show a decrease of the D1 peak area associated
175 with a decrease in the width of the G band, resulting in a decrease of the R2 ratio (Fig. 1b).
176 This trend in the R2 ratio is compatible with a T_{\max} increase in the metamorphic samples
177 (Beysac et al., 2007; Lanari et al., 2012). The T_{\max} estimates by RSCM thermometry range
178 from $330 \pm 20^{\circ}\text{C}$ to $520 \pm 20^{\circ}\text{C}$ (Table 1). The projection of the estimated T_{\max} along a WSW
179 to ENE profile (XX' in Fig. 1c) shows a progressive increase of T_{\max} . This increase in
180 temperature is compatible with the metamorphic gradient already proposed by Tricart and
181 Schwartz (2004) in the studied area. The temperature increase from west to east is also
182 consistent with the increase in pressure along a low-temperature subduction-related
183 geothermal gradient (Goffé et al., 2004; Lardeaux et al., 2006, Angiboust et al., 2012). This
184 relationship allows us to associate a pressure maximum with the T_{\max} estimated by RSCM.
185 The sub-greenschist facies domain of the Chenaillet massif corresponds to a P-T range of $P < 4$
186 kbar and $T \sim 200\text{-}300^{\circ}\text{C}$. The LT-blueschist domain corresponds to P-T conditions of $P = 9\text{-}$
187 11 kbar and $320 < T < 360^{\circ}\text{C}$; the MT-blueschist domain indicates P-T conditions of $10\text{-}12$
188 kbar and $340\text{-}390^{\circ}\text{C}$; the HT-blueschist domain corresponds to P-T conditions of $12 < P < 15$
189 kbar and $380 < T < 470^{\circ}\text{C}$; and the eclogitic domain indicates conditions of $20 < P < 26$ kbar
190 and $480 < T < 520^{\circ}\text{C}$.

191 5. XRD serpentinites characterization

192 5.1. Experimental conditions

193 The < 2 mm fraction of the serpentinite samples was powdered using a McCrone
194 micronizing mill and washed with H_2O . The resulting slurry was centrifuged and freeze-dried
195 before being prepared as a randomly oriented mount. The XRD patterns were recorded with a
196 Bruker D5000 powder diffractometer equipped with a SolX Si(Li) solid state detector from
197 Baltic Scientific Instruments using $\text{CuK}\alpha$ 1+2 radiation. The intensities were recorded at

198 0.04° 2-theta step intervals from 5 to 90° (5 s counting time per step) for bulk serpentinite
199 mineralogy determination. The XRD detection level was approximately one percent (< 1%).

200 5.2. Results

201 The XRD results and the mineralogical assemblages are presented in Figure 2 and
202 Table 2. All of the XRD lines of the samples are dominated by serpentine minerals
203 (serpentine species > 90%) associated with magnetite (Fig. 2). Brucite is not observed;
204 however, mineral species are not detected below a concentration of 1 wt%. The serpentinite
205 sampled in the Chenaillet massif (ICH2) is composed of serpentine, magnetite, chlorite and
206 rare magmatic clinopyroxene. The serpentinites sampled in the LT-blueschist (CR02) and
207 MT-blueschist (RQ23 and RQ16) domains present mineralogical assemblages dominated by
208 serpentine and minor magnetite. In Sample RQ16, chlorite is detected. The serpentinites from
209 the HT-blueschist (BB01 and RQ01) and eclogitic (Vi01) domains are composed of
210 serpentine, metamorphic olivine and magnetite. The mineral antigorite is detectable in the
211 XRD spectrum of Sample BB01 (Fig. 2 and Table 2). The presence of olivine is related to the
212 onset of antigorite destabilization during the dehydration reaction (Evans, 2004). This
213 secondary olivine appears in Samples RQ01 and Vi01. In Sample Vi01, clinopyroxene and
214 chlorite are detected, in accordance with the microscopic observations (Auzende et al., 2006).
215 To precisely identify the varieties of serpentines, we used Raman spectroscopy coupled with
216 microscopic observations.

217 6. Serpentine characterizations

218 6.1. Raman spectrometry

219 The different serpentine species have been characterized by Raman spectroscopy
220 coupled with petrographic observations of polished thin-sections of serpentinites. The Raman
221 signal was acquired over approximately 90 s in three accumulating cycles, with a laser output
222 power on the sample surface adjusted between 10 and 20 mW. The spectral resolution was 1
223 cm^{-1} using 1800 lines/mm grating. A reproducibility of 1 cm^{-1} was attained on successive
224 spectra of a given mineral sample. The spectral regions from 150 to 1150 cm^{-1} and from 3600
225 to 3720 cm^{-1} were investigated because they include the lattice vibrational modes and the OH
226 stretching mode region that is characteristic of serpentine species, respectively (Rinaudo et al.,
227 2003; Auzende et al., 2004; Groppo et al., 2006).

228 The bands detected in these spectral regions are indicative of the crystalline structure of the
229 sample. For each spectra, the assignment of the band position and the full width at half
230 maximum were determined using the Peakfit© software.

231 In the low wavenumber region, four main peaks (near 230, 390, 690 and 1100 cm^{-1})
232 characterize the spectra of lizardite and chrysotile (Fig. 3a). Intense peaks specific to the
233 antigorite spectrum occur at lower wavenumbers (226, 373, 680 and 1043 cm^{-1}) and are much
234 broader than those corresponding to other serpentines (Fig. 3b). The differences between
235 chrysotile and lizardite spectra, although small, can be clearly identified by the sharpness of
236 the Raman lines. In particular, a single band at 1100 cm^{-1} is observed in chrysotile, whereas
237 several convoluted bands are observed between 1060 and 1100 cm^{-1} in lizardite (Fig. 3a). In
238 the high wavenumber region, the convoluted vibrational modes attributed to the OH stretching
239 of serpentine are located between 3600 and 3720 cm^{-1} . In chrysotile, the most intense band
240 occurs at 3697 cm^{-1} , with a distinct shoulder at 3690 cm^{-1} and a weak band at 3648 cm^{-1} .
241 Lizardite has a markedly different spectrum (Fig. 3a): the most intense band occurs at a lower
242 frequency (minimum at 3680 cm^{-1}) with a well-defined high frequency band at 3703 cm^{-1} . In
243 antigorite, the spectra are characterized by a broad band at 3670 cm^{-1} and a sharp band at
244 3700 cm^{-1} (Fig. 3b). Mixed lizardite/antigorite spectra are also observed (Fig. 3c). In the low
245 wavenumber region, the peak at 1043 cm^{-1} is present (as in antigorite), but the peak at 373 cm^{-1}
246 is shifted to $\sim 380 \text{ cm}^{-1}$ (toward the classical $\sim 390 \text{ cm}^{-1}$ peak of lizardite). In the high
247 wavenumber region, the second “antigorite” peak at 3700 cm^{-1} is still present, but the most
248 intense peak is located between 3670 cm^{-1} and 3680 cm^{-1} , in an intermediate position between
249 the most intense “antigorite” and “lizardite” peaks (Fig. 3c).

250 6.2. Petrology

251 The repartition of the serpentine species correlates with the T_{max} along the XX' profile
252 (Fig. 1c). Lizardite dominates in the greenschist and LT-blueschist facies (from $< 300^\circ\text{C}$ to
253 360°C), while antigorite progressively appears in the LT-blueschist facies. Antigorite
254 becomes progressively dominant in the MT-blueschist facies ($340\text{-}390^\circ\text{C}$), ultimately
255 becoming the sole serpentine species in the HT-blueschist and eclogite facies ($T > 380^\circ\text{C}$).
256 Chrysotile is observed in all of the high pressure serpentinite samples, filling in the late cracks
257 or micro-fractures related to the samples' final exhumation at the ductile/brittle transition. In
258 the following paragraphs, we detail the mineralogy and texture of the serpentinites according

259 to the degree of metamorphism. The T_{\max} for each serpentinite sample refers to the T_{\max}
260 estimated from the associated metasediments.

261 Sample ICH2 ($T < 300^{\circ}\text{C}$) is characterized by the development of a mesh texture underlined
262 by magnetite, which suggests the classical reaction of olivine + water = serpentine (mesh) +
263 magnetite \pm brucite (Figs 4a and 4a'). The Raman spectrometry shows that lizardite is the
264 dominant serpentine species. Locally, the mesh is crosscut by secondary chrysotile veins.

265 Sample CR02 ($T_{\max} = 340^{\circ}\text{C}$) shows a mesh texture consisting of lizardite surrounded by
266 magnetite (Figs 4b and 4b'). Locally, secondary antigorite (representing less than 10% of the
267 matrix) crystallized at the boundaries of relict brownish lizardite crystals. We assign the
268 lizardite crystallization to the sea-floor metamorphism (oceanic serpentinization) and the
269 antigorite crystallization to the LT-blueschist metamorphism.

270 Sample RQ23 ($T_{\max} = 356^{\circ}\text{C}$) is equally composed of antigorite and relics of lizardite (Figs 4c
271 and 4c'). The antigorite crystallized at the grain boundaries of the lizardite relics and as
272 millimeter-sized antigorite patches with an interlocking texture. The lizardite relics present
273 the typical mixed lizardite-antigorite Raman spectra, suggesting the partial mineral
274 replacement of oceanic lizardite by metamorphic micrometric antigorite. Magnetite locally
275 underlines the original mesh texture.

276 Sample RQ16 ($T_{\max} = 373^{\circ}\text{C}$) shows the same mineral relationship as Sample RQ23, with
277 some relics of lizardite that have a mixed character between antigorite and lizardite (Figs 4d
278 and 4d'). The antigorite that developed at the grain boundaries enlarged and the blades of
279 antigorite crystallized. In this sample, the proportion of magnetite decreased, but chlorite
280 crystallized (Fig. 2), which suggests the development of chlorite at the expense of magnetite
281 in the presence of aluminum.

282 Sample BB01 ($T_{\max} = 402^{\circ}\text{C}$), coming from the HT-blueschist unit, is composed only of
283 antigorite and a string of magnetite that underlies the previous oceanic mesh texture (Figs 5a
284 and 5a'). The patches are composed of sub-millimetric interlocking blades of antigorite. The
285 presence of antigorite is readily detectable in the XRD spectra (Fig. 2).

286 In Sample RQ01 ($T_{\max} = 463^{\circ}\text{C}$), only antigorite serpentine is observed (Figs. 5b and 5b').
287 The mesh, still underlined by magnetite and bastite (free of magnetite), remains preserved,
288 which suggests a static crystallization of antigorite at the expense of oceanic lizardite. The
289 olivine peak appears in the XRD spectra.

290 In Sample Vi01 ($T_{\max} = 498^{\circ}\text{C}$), antigorite is again the sole serpentine species (Figs. 5c and
291 5c'). Similar to Sample RQ01, the pseudomorphic texture (mesh and bastite) is preserved and
292 underlined by magnetite, but antigorite blades of a few hundred microns have started to
293 obliterate the mesh texture. In this sample, we observed olivine and chlorite signals in the
294 XRD spectra (Fig. 2).

295 6.3. Electron microprobe

296 In addition, the major element concentrations of the serpentine species were acquired
297 using a Cameca SX100 electron microprobe at the “Laboratoire Magma et Volcans”
298 (Clermont Ferrand, France). The operating conditions were as follows: an accelerating voltage
299 of 15 kV, a sample current of 15 nA and a counting time of 10 s/element, except for Ni (20 s).
300 The standards used were albite (Na), forsterite (Mg), orthoclase (K), wollastonite (Ca and Si),
301 MnTiO_3 (Ti and Mn), Cr_2O_3 (Cr), fayalite (Fe), olivine (Ni), and synthetic Al_2O_3 (Al).
302 Representative analyses are reported in Table 3. Serpentine phases can contain over 13 wt%
303 of water in their crystal structure. The volatile content is not always correlated with the degree
304 of serpentinization because other phases (e.g., talc, brucite, chlorite, clay minerals) associated
305 with serpentine minerals can influence this measurement. In the studied samples, the volatile
306 content (100% – wt% major elements) varies from 12.54 to 15.67 wt% (Table 3). We did not
307 observe any correlation between the volatile content in the serpentine minerals and the degree
308 of metamorphism. However, we did observe a relationship between the homogenization of the
309 serpentine composition and the degree of metamorphism (Fig. 6). When plotted on the SiO_2
310 vs. Al_2O_3 field, the lower metamorphic samples are scattered, while the higher metamorphic
311 samples are grouped closer to the end-member antigorite composition (Fig. 6), with 44 wt%
312 SiO_2 and 1.03 wt% Al_2O_3 (Deer et al., 1992). The samples with an intermediate degree of
313 metamorphism, dominated by mixed lizardite/antigorite, fall between the lizardite and
314 antigorite fields. It is also noticeable that the Al_2O_3 content decreases and the SiO_2 content
315 increases with the degree of metamorphism (Fig. 6). This increase of SiO_2 in serpentine is
316 correlated with a slight increase of whole-rock SiO_2 content, from ~39.4 wt% at grade 0 to
317 ~40.5 wt% (Lafay et al., in press).

318 7. Discussion

319 7.1. Lizardite to antigorite transitions

320 The aim of this study is to develop a combined mineral investigation of serpentinites
321 and compare the results with T_{\max} estimates from associated metasediments. This approach
322 allows us to indirectly constrain the P-T conditions of the phase changes in natural
323 serpentinites and to compare our results with previous experimental works. Moreover, most of
324 the published results concerning the changes from lizardite/chrysotile to antigorite are
325 acquired through experiments performed at intermediate pressures of approximately 6-7 kbar
326 (e.g., O'Hanley (1996)); our samples allow us to characterize this transition at higher pressures
327 (between 4 and 26 kbar) that are pertinent to the P-T conditions in subduction zones. Our
328 study highlights the following important points:

329 1-The early serpentinization stage is related to the hydrothermalism of the oceanic lithosphere
330 and generates lizardite-bearing mesh textures (Figs. 7a and 7b).

331 2-In the lowest-grade metamorphic units (sub-greenschist facies; $P < 4$ kbar; $T \sim 200$ - 300°C),
332 antigorite is absent and lizardite is the dominant phase. Such observations are in agreement
333 with previous experimental results (e.g., Evans, 2004).

334 3-In polymetamorphic weakly deformed domains, the oceanic mesh textures are preserved in
335 all peak P-T conditions (Fig. 7b). At the initial stages, antigorite appears along the lizardite
336 grain boundaries (Fig. 7c) and at more evolved stages overprints lizardite (Fig. 7d), preserving
337 the initial textures (mesh and bastite). This observation argues against the commonly
338 proposed idea that antigorite preferentially crystallizes within deformed domains (Miyashiro
339 et al., 1969).

340 4-Antigorite crystallizes in two distinct crystallographic sites. Antigorite first appears in LT-
341 blueschist at 320°C at the lizardite grain boundary, forming a network of veins (Fig. 7c).
342 These veins grow with the degree of metamorphism, from ~ 20 μm up to 150 μm (Fig. 7d) in
343 the MT-blueschist facies (up to 390°C). Such crystallization texture is typical of mineral
344 replacement by dissolution-precipitation processes in the presence of a free fluid (Putnis,
345 2009; Lafay et al., 2012).

346 The second crystallographic site is where antigorite crystallizes in the cores of lizardite grains
347 in MT-blueschist facies conditions (Fig. 7d). Raman spectrometry shows mixed
348 lizardite/antigorite spectra, suggesting an intimate association of lizardite and antigorite at the
349 micron-scale (Fig. 7a). This intimate mineral association suggests a solid-state transition (Eda
350 et al., 2006). The solid-state crystallization of antigorite at the expense of lizardite is partial

351 between 340 and 380°C and complete above in HT-blueschist and eclogitic facies conditions
352 (Figs. 7a and 7e).

353 7.2. Lizardite to antigorite reactions

354 In the literature, it is typically proposed that the thermal stability fields of antigorite
355 and lizardite overlap between temperatures of 250 and 500°C, while chrysotile is metastable
356 (e.g., Evans, 2004). We can refine the relative stability fields of lizardite and antigorite from
357 our observations of high-pressure natural samples. It is well known that serpentinization is a
358 complex process controlled by time- and site-dependent variables such as fluid/rock ratios,
359 silica activity, oxygen fugacity and pH (Evans, 2004; Frost and Beards, 2007). Lizardite and
360 antigorite are co-stable (or at least the lizardite is not completely destabilized) between 320
361 and 390°C for pressures greater than 9 kbar (Fig. 7). It is noticeable that below 300°C and 4
362 kbar, antigorite is not observed. This observation contradicts the phase diagram of O'Hanley
363 (1996), in which antigorite appears at 250°C at low pressures, and suggests that antigorite
364 crystallization is not only temperature dependent but also may be pressure dependent (Ulmer
365 and Trommsdorff, 1995; Wunder and Schreyer, 1997).

366 Thermodynamic work on the serpentinite multisystem predicts the crystallization of antigorite
367 (Atg) at the expense of chrysotile (Chr) or lizardite (Lz), according to the following reactions
368 (Evans, 2004) with forsterite (Fo) and brucite (Brc):

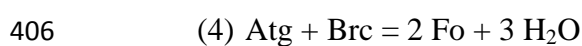


372 Reactions (1) and (2) are thermodynamically favorable for temperatures between 300 and
373 400°C (Fig. 8), while at lower temperatures, the conversion of lizardite to antigorite is
374 thermodynamically more efficient with a modest introduction in the serpentinite multisystem
375 of SiO₂ (e.g., Evans, 2004). Brucite is not detected as a byproduct of antigorite; however, we
376 can conclude that brucite is not present in the studied samples below the XRD concentrations
377 (< 1 wt%), although brucite is detected in the Monviso serpentinites (Debret, pers. com.). The
378 absence of brucite could be interpreted either as the result of a lower olivine hydration with
379 respect to enstatite hydration (precluding the release of Mg necessary to the brucite
380 crystallization) or as the consumption of brucite during prograde reactions. Metamorphic

381 olivine is rare and observed in the studied samples at temperatures higher than 460°C. Thus,
382 Reactions (1) and (2) cannot explain the crystallization of antigorite at low temperatures (<
383 330°C according to Evans (2004)). In contrast, we clearly observe the direct crystallization of
384 veins of antigorite at the expense of lizardite starting at 320°C in the presence of
385 metasediments. Moreover, we observe a general enrichment in SiO₂ throughout the antigorite
386 (Fig. 6) that is correlated with a whole-rock SiO₂ enrichment along the metamorphic gradient
387 (Lafay et al., in press). This finding suggests the onset of antigorite crystallization at 320°C,
388 assisted by SiO₂-rich fluids, according to Reaction (3), by dissolution-precipitation processes
389 (Fig. 8). Rüpke et al. (2004) have shown that above a depth of 50 km (T < 300°C), oceanic
390 sediments release almost 50% of their initial water content. This fluid is enriched in volatile
391 elements and silica and potentially hydrated the mantle wedge (e.g., Bebout and Barton, 1989;
392 Bebout et al., 1999). Fluid exchange between the subducted oceanic sediments and our
393 serpentinite samples is clearly demonstrated by the enrichment of volatile elements,
394 particularly in the antigorite (Lafay et al., in press). Thus, the most favorable circumstances
395 for silicification are waters that are equilibrated with sedimentary rocks in the Alpine wedge
396 and that percolated into the serpentinites, as observed in the Catalina Schist in California
397 (Bebout and Barton, 1989, Bebout et al., 2004).

398 As already discussed, we also observed the solid-state transformation of lizardite into
399 antigorite, suggesting the progression of Reaction (1) between 340 and 380°C. In the natural
400 samples presented here, this reaction occurred at slightly higher temperatures than were
401 predicted by thermodynamic calculations (260-310°C at 10 kbar, Evans, 2004).

402 At a minimum temperature of 460°C, secondary olivine crystallized (Fig. 2), which suggests
403 the onset of antigorite destabilization. This is compatible with a decrease of the whole-rock
404 L.O.I from 13 wt% to < 12 wt% (Lafay et al., in press). According to Evans (2004), it
405 corresponds to the reaction:



407 In the natural samples studied, this reaction occurred at $\geq 460^\circ\text{C}$ and $P > 12 \text{ kbar}$, as
408 predicted by thermodynamic calculations (Evans, 2004). However, this reaction involves
409 brucite, which we did not detect in the samples. Thus, we propose that the brucite produced
410 by Reaction (1) at lower temperatures is completely consumed by Reaction (4) along the
411 subduction gradient (Fig. 8).

412 **8. Conclusion**

413 Raman spectroscopy and XRD are efficient methods for identifying different species
414 of serpentine because serpentine optical identification is difficult. In addition, various
415 serpentine species are often interpenetrated, and Raman micro-spectrometry proves to be a
416 useful micro-characterization tool for resolving structural differences at the scale of the
417 various grain generations. The application of these methods to samples from the Alps shows
418 that lizardite is preserved under sub-greenschist facies conditions in oceanic environment and
419 ophiolites. Antigorite progressively replaces lizardite under LT- to MT-blueschist facies
420 conditions (320-390°C) and is the sole serpentine phase under HT-blueschist to eclogites
421 facies conditions (> 380°C). Our study shows several generations of serpentine in sea-floor
422 and metamorphic processes. Below 320°C, lizardite and chrysotile are the only stable
423 serpentine species. Between 320°C and 390°C, lizardite and antigorite coexist and antigorite
424 develops at the expense of lizardite through two processes. Antigorite first appears at the
425 lizardite grain boundaries through dissolution-precipitation processes in the presence of SiO₂.
426 We propose that this fluid comes from the local dehydration of the surrounding
427 metasediments in subduction environments. Antigorite also crystallizes in the cores of the
428 lizardite mesh through solid-state transitions at slightly higher temperatures, between 340°C
429 and 380°C. This transition is characterized by mixed lizardite/antigorite Raman spectra.
430 Above 390°C and 12 kbar, lizardite is absent and antigorite is the only stable serpentine
431 species. Above 460°C, antigorite begins to destabilize into olivine. We did not detect
432 brucite in any of the studied samples, although this mineral is theoretically involved in the
433 transition from lizardite to antigorite. We propose that the brucite produced at low
434 temperatures is consumed at higher temperatures and remains a transition phase. This process
435 would explain why brucite is rarely observed in natural samples in oceanic and subduction
436 environments worldwide.

437 **9. Acknowledgments**

438 This study was supported by the *Agence Nationale de la Recherche* project n° ANR-08-
439 BLAN-0303-01 “Erosion and Relief Development in the Western Alps”, the SUBDEF grant
440 n° ANR-08-BLAN-0192 and the Labex OSUG2020. N. Findling is thanked for the XRD
441 analyses (University of Grenoble 1).

442

443 **10. References**

- 444 Agard, P., Monié, P., Jolivet, L., and Goffé, B., 2002. Exhumation of the Schistes Lustrés
445 complex: In situ laser probe Ar-40/Ar-39 constraints and implications for the western Alps.
446 *Journal of Metamorphic Geology* 20, 599-618.
- 447 Agard, P., Vidal, P., Goffé, B., 2001. Interlayer and Si content of phengite in HP-LT
448 carpholite-bearing metapelites. *Journal of Metamorphic Geology* 19, 479-495.
- 449 Alt, J.C., Shanks, W.C., 2003. Serpentinization of abyssal peridotites from the MARK area,
450 Mid-Atlantic ridge, sulphur geochemistry and reaction modelling. *Geochimica Cosmochimica*
451 *Acta* 67, 641-653.
- 452 Andréani, M., Mével, C., Boullier, A.M., Escartin, J., 2007. Dynamic control on serpentine
453 crystallisation in veins: constraints on hydration processes in oceanic peridotites.
454 *Geochemistry Geophysics Geosystems* Q02012, doi: 10.1029/2006GC001373.
- 455 Angiboust, S., Langdon, R., Agard, P., Waters, D., Chopin C., 2012. Eclogitization of the
456 Monviso ophiolite (W. Alps) and implications on subduction dynamics. *Journal of*
457 *Metamorphic Geology* 30, 37-61.
- 458 Auzende, A.L., Guillot, S., Devouard, B., Baronnet, A., 2006. Serpentinites in Alpine
459 convergent setting: Effects of metamorphic grade and deformation on microstructures.
460 *European Journal of Mineralogy* 18, 21-33.
- 461 Auzende, A.L., Daniel, I., Reynard, B., Lemaire, C., Guyot, F., 2004. High-pressure
462 behaviour of serpentine minerals: a Raman spectroscopic study. *Physics and Chemistry of*
463 *Minerals* 31(5), 269-277.
- 464 Auzende, A.L., Devouard, B., Guillot, S., Daniel, I., Baronnet, A., Lardeaux, J.M., 2002.
465 Serpentinites from Central Cuba: petrology, and HRTEM study. *European Journal of*
466 *Mineralogy* 14, 905-914.
- 467 Bard, D., Yarwood, J., Tylee, B., 1997. Asbestos fibre identification by Raman
468 microspectroscopy. *Journal of Raman Spectroscopy* 28, 803-809.
- 469 Baronnet, A., Belluso, E., 2002. Microstructures of the silicates: key information about
470 mineral reactions and a link with the Earth and materials sciences. *Mineralogical Magazine*
471 66, 709-732.
- 472 Bebout, G.E., Ryan, J.G., Leeman, W.P., Bebout, A.E., 1999. Fractionation of trace elements
473 by subduction-zone metamorphism, effect of convergent-margin thermal evolution. *Earth and*
474 *Planetary Science Letters* 171, 63-81.
- 475 Bebout, G.E., Barton, M.K., 1989. Fluid flow and metasomatism in a subduction zone
476 hydrothermal system: Catalina Schist terrane, California. *Geology* 17, 976-980.

477 Beyssac, O., Goffé, B., Chopin, C., Rouzaud, N., 2002. Raman spectra of carbonaceous
478 material in metasediments : a new geothermometer. *Journal of Metamorphic Geology* 20,
479 859-871.

480 Beyssac, O., Goffé, B., Petitet, J.P., Froigneux, E., Moreau, M., Rouzaud, J.N., 2003. On the
481 characterisation of disordered and heterogeneous carbonaceous materials by Raman
482 spectrometry. *Spectrochimica Acta* 59, 2267-2276.

483 Beyssac, O., Simoes, M., Avouac, J.P., Farley, K.A., Chen Y.G., Goffé, B., 2007. Late
484 Cenozoic metamorphic evolution and exhumation of Taiwan. *Tectonics* 26 TC6001, pp. 32.

485 Boudier, F., Baronnet, A., Mainprice, D., 2010. Serpentine mineral replacements of natural
486 olivine and their seismic implications : oceanic lizardite versus subduction-related antigorite.
487 *Journal of Petrology* 51, 495-512.

488 Bromiley, G.D., Pawley, A.R. 2003. The stability of antigorite in the systems MgO-SiO₂-H₂O
489 (MSH) and MgO-Al₂O₃-SiO₂-H₂O (MASH): The effects of Al³⁺ substitution on high-pressure
490 stability. *American Mineralogist* 88, 99-108.

491 Deer, W.A., Howie, R.A., Zussman, J., 1992. An introduction to the rock-forming minerals,
492 2nd edition. Longman Scientific & Technical, Harlow.

493 Deville, E., Fudral, S., Lagabrielle, Y., Marthaler, M., Sartori, M., 1992. From oceanic closure
494 to continental collision: A synthesis of the Schistes lustrés metamorphic complex of the
495 western Alps. *Geological Society of America Bulletin* 104, 127-139.

496 Dumont T., Schwartz S., Guillot S., Simon-Labric T., Tricart P., Jourdan S., 2012. Structural
497 and sedimentary records of the Oligocene revolution in the Western Alps. *Journal of*
498 *Geodynamics* 56-57, 18-38.

499 Eda, K., Uno, Y., Nagai, N., Sautani, N., Chen, C., Whittingham, M.S., 2006. Structure-
500 inheriting solid-state reactions under hydrothermal conditions. *Journal of Solid State*
501 *Chemistry* 179, 1453-1458.

502 Evans, B.W., 2004. The Serpentinite Multisystem Revisited: Chrysotile is Metastable.
503 *International Geology Review* 46, 479-506.

504 Frost, B.R., Beard, J.S., 2007. On silica activity and serpentinization. *Journal of Petrology* 49,
505 1351-1368.

506 Ganne, J., Bertrand, J.M., and Fudral, S., 2005. Fold interference pattern at the top of
507 basement domes and apparent vertical extrusion of HP rocks (Ambin and South Vanoise
508 massifs, western Alps). *Journal of Structural Geology* 27, 553-570.

509 Goffé, B., Schwartz, S., Lardeaux, J.M., Bousquet, R., 2004. Metamorphic structures of the
510 Western and Ligurian Alps. *Mitteilungen der Österreichischen Mineralogischen Gessellschaft*
511 149, 125-144.

- 512 Groppo, C., Compagnoni, R., 2007. Metamorphic veins from the serpentinites of the
513 Piemonte Zone, western Alps, Italy: a review. *Periodico di Mineralogia* 76, 127-153.
- 514 Groppo, C., Rinaudo, C., Cairo, S., Gastaldi, D., Compagnoni, R., 2006. Micro-Raman
515 spectroscopy for quick and reliable identification of serpentinite minerals from ultramafics.
516 *European Journal of Mineralogy* 18, 319-329.
- 517 Guillot, S., Hattori, K., Agard, P., Schwartz, S., Vidal, O., 2009. Exhumation processes in
518 oceanic and continental subduction contexts: a review. In S. Lallemand and F. Funiciello
519 (eds.) "Subduction Zone Dynamics", Springer-Verlag Berlin Heidelberg. doi: 10.1007/978-3-
520 540-87974-9, 175-204.
- 521 Hattori, K., Guillot, S., 2007. Geochemical character of serpentinite associated with high to
522 ultrahigh pressure rocks in Alps, Cuba and the Himalayas: recycling of elements in
523 subduction zones. *Geochemistry Geophysics Geosystems* Q09010,
524 doi:10.1029/2007GC001594.
- 525 Klopogge, J.T., Frost, R.L., Rintoul, L., 1999. Single crystal Raman microscopic study of the
526 asbestos mineral chrysotile. *Journal of Physical Chemistry* 1, 2559-2564.
- 527 Komabayashi, T., Hirose, K., Funakoshi, K., Takafuji, N., 2005. Stability of phase A in
528 antigorite (serpentine) composition determined by in situ X-ray pressure observations. *Physics*
529 *of the Earth and Planetary Interiors* 151, 276-289.
- 530 Lanari P., Guillot S., Schwartz S., Vidal O., Tricart P., Riel N., Beyssac O., 2012.
531 Diachronous evolution of the alpine continental wedge: evidences from P-T estimates in the
532 Briançonnais Zone houillère (France-Western Alps). *Journal of Geodynamics* 56-57, 39-54.
- 533 Lagabrielle, Y., and Polino, R., 1988. Un schéma structural du domaine des Schistes lustrés
534 ophiolitifère au nord-ouest du massif du Mont Viso (Alpes Sud-Occidentales) et ses
535 implications. *Comptes Rendus de l'Académie des Sciences* 306, 921-928.
- 536 Lafay, R., Montes-Hernandez, G., Janots, E., Chiriac, R., Findling, N., Toche, F., 2012.
537 Mineral replacement rate in olivine by chrysotile and brucite under high alkaline conditions.
538 *Journal of Crystal Growth* 347, 62-72.
- 539 Lafay R., Deschamps F., Schwartz S., Guillot S., Godard M., Nicollet C. High-pressure
540 serpentinites, a trap-and-release system controlled by metamorphic conditions : Example from
541 the Piedmont zone of the western Alps. *Chemical Geology*. In press.
- 542 Lardeaux, J.M., Schwartz, S., Paul, A., Tricart, P., Guillot, S., Béthoux, N., Masson, F., 2006.
543 A crustal-scale cross section of the southwestern Alps combining geophysical and geological
544 imagery. *Terra Nova* 18, 412-422.
- 545 Lemoine, M., Tricart, P., Boillot, G., 1987. Ultramafic and gabbroic ocean floor of the
546 Ligurian Tethys (Alps, Corsica, Apennines): in search of a genetic model. *Geology* 15, 622-
547 625.

- 548 Lewis, I., Chaffin, N., Gunter, M., Griffiths, P., 1996. Vibration spectroscopic studies of
549 asbestos and comparison of suitability for remote analysis. *Spectrochimica Acta Part A* 52,
550 315-328.
- 551 Li, X.P., Rahn, M., Bucher, K., 2004. Serpentinites of the Zermatt-Saas ophiolite complex
552 and their texture evolution. *Journal of Metamorphic Geology* 22, 159-177.
- 553 Mellini, M., Ferraris, G., Compagnoni, R., 1985. Carlosturanite: HRTEM evidence of a
554 polysomatic series including serpentine. *American Mineralogist* 70, 773-781.
- 555 Mével, C., Caby, R., Kienast, J.R., 1978. Amphibolite facies conditions in oceanic crust:
556 example of amphibolitized flaser gabbros and amphibolites from the Chenaillet ophiolite
557 massif (Hautes Alpes, France). *Earth and Planetary Science Letters* 39, 98-108.
- 558 Miyashiro, A., Shido, F., Ewing, M., 1969. Composition and origin of serpentinites from the
559 Mid-Atlantic Ridge near 24 and 30°N. *Contribution to Mineralogy and Petrology* 23, 117-
560 127.
- 561 O'Hanley, D.S., 1996. *Serpentinites: Oxford Monographs on Geology and Geophysics* 34,
562 277p
- 563 Padron-Navarta, J.A., Sanchez-Vizcaino, V.L., Garrido, C.J., Gómez-Pugnaire, M.T.,
564 Jabaloy, A., Capitani, G.C., Mellini, M., 2008. Highly ordered antigorite from Cerro del
565 Almiraz HP-HT serpentinites, SE Spain. *Contribution to Mineralogy and Petrology* 156, 679-
566 688.
- 567 Padron-Navarta, J.A., Hermann, J., Garrido, C.J., Sanchez-Vizcaino, V.L., Gómez-Pugnaire,
568 M.T., 2010. An experimental investigation of antigorite dehydration in natural silica-enriched
569 serpentine. *Contribution to Mineralogy and Petrology* 159, 25-42.
- 570 Perrillat, J.P., Daniel, I., Koga, K.T., Reynard, B., Cardon, H., Crichton, W.A., 2005. Kinetics
571 of antigorite dehydration: A real-time X-ray diffraction study. *Earth and Planetary Science*
572 *Letters* 236, 899-913.
- 573 Putnis, A., 2009. Mineral replacement reactions. *Reviews in Mineralogy and Geochemistry*
574 70, 87-124.
- 575 Quirico, E., Montagnac, G., Rouzaud, J.N., Bonal, L., Bourot-Denise, M., Dufer, S., Reynard,
576 B., 2009. Precursor and metamorphic condition effects on Raman spectra of poorly ordered
577 carbonaceous matter in chondrites and coals. *Earth and Planetary Science Letters* 287, 185-
578 193.
- 579 Reynard, B., Wunder, B., 2006. High-pressure behavior of synthetic antigorite in the MgO-
580 SiO₂-H₂O system from Raman spectroscopy. *American Mineralogist* 91, 459-462.
- 581 Rinaudo, C., Gastaldi, D., Belluso, E., 2003. Characterization of chrysotile, antigorite, and
582 lizardite by FT-Raman spectroscopy. *Canadian Journal of Mineralogy* 41, 883-890.

583 Rosenbaum, G., Lister, G.S., 2005. The Western Alps from the Jurassic to Oligocene: spatio-
584 temporal constraints and evolutionary reconstructions. *Earth Science Reviews* 69, 281-306.

585 Rüpke, L.H., Morgan, J.P., Hort, M., Connolly, J.A., 2004. Serpentine and the subduction
586 water cycle. *Earth and Planetary Science Letters* 223, 17-34.

587 Scambelluri, M., Müntener, O., Hermann, J., Piccardo, G.B., Trommsdorff, V., 1995.
588 Subduction of water into the mantle-history of an alpine peridotite. *Geology* 23, 459-462.

589 Schwartz, S., Tricart, P., Lardeaux, J.M., Guillot, S., Vidal, O., 2009. Final exhumation of an
590 accretionary wedge (Queyras Schistes Lustrés, Western Alps): deformation sequence and
591 associated P-T-t path. *Geological Society of America Bulletin* 121, 502-518.

592 Schwartz, S., Lardeaux, J.M., Tricart, P., Guillot, S., Labrin, E., 2007. Diachronous
593 exhumation of subducted HP metamorphic rocks from southwestern Alps: evidences from
594 fission-track analysis. *Terra Nova* 19, 133-140.

595 Schwartz, S., Allemand, P., Guillot, S., 2001. Numerical model of the effect of serpentinites
596 on the exhumation of eclogitic rocks: insights from the Monviso ophiolitic massif (Western
597 Alps). *Tectonophysics* 42, 193-206.

598 Schwartz, S., Lardeaux, J.M., Guillot, S., Tricart, P., 2000. The diversity of eclogitic
599 metamorphism in the Monviso ophiolitic complex, western Alps, Italy. *Geodinamica Acta* 13,
600 169-188.

601 Spear, F.S., 1993, *Metamorphic phase equilibria and pressure-temperature-time paths:*
602 *Washington, D.C., Mineralogical Society of America, 799 p.*

603 Tricart, P., 1984. From passive margin to continental collision: A tectonic scenario for the
604 western Alps. *American Journal of Science* 284, 97-120.

605 Tricart, P., Lemoine, M., 1986. From faulted blocks to megamullions and megaboudins-
606 Tethyan heritage in the structure of the western Alps. *Tectonics* 5, 95-118.

607 Tricart, P., Schwartz, S., 2006. A north - south section across the Queyras Schistes lustrés
608 (Piedmont zone, Western Alps): syncollision refolding of a subduction wedge. *Eclogae
609 Geologicae Helvetiae* 99, 429-442.

610 Trommsdorff, V., Sanchez-Vizcaino, V.L., Gomez-Pugnaire, M.T., Müntener, O., 1998. High
611 pressure breakdown of antigorite to spinifex-textured olivine and orthopyroxene, SE Spain.
612 *Contribution to Mineralogy and Petrology* 132, 139-148.

613 Ulmer, P., Trommsdorff, V., 1995. Serpentinite stability to mantle depths and subduction
614 related magmatism. *Science* 268, 858-861.

615 Wicks, F.J., O'Hanley, D.S., 1988. Serpentine minerals: Structures and petrology. *Rev
616 Mineral*, 19, In S. W. Bailey Ed., *Hydrous Phyllosilicates*, pp. 91-167

617 Wunder, B., Schreyer, W., 1997. Antigorite: High Pressure stability in the system MgO-SiO₂-
618 H₂O (MSH). *Lithos* 41, 213-227.

619

620 **Figure captions**

621 Fig. 1. (a) Tectonic sketch map of the southwestern Alps, and T_{\max} results of metasediments
622 obtained by the RSCM method. Seven serpentinites were sampled along the paleo-subduction
623 zone from sub-greenschist (Chenaillet) to eclogitic (Monviso) facies conditions. (b)
624 Characteristic evolution of Raman spectra from selected metasediments. Positions of the
625 graphite G band and D1, D2, D3 defect bands are indicated. For each spectrum, the value of
626 the mean R2 ratio ($R2=D1/[G+D1+D2]$ peak area ratio) is given (see Table 1). (c) T_{\max} results
627 projected onto a WSW – ENE cross section (XX').

628

629 Fig. 2. XRD patterns of serpentinites. The mineralogy is dominated by a magnetite and
630 serpentine assemblage. The antigorite peaks (black star) and olivine (Ol) appear in samples
631 RQ01 and Vi01. The presence of olivine is due to the onset of antigorite destabilization into
632 olivine.

633

634 Fig. 3. Raman spectra acquired from different varieties of serpentine from the study area in
635 low frequency ($150-1150\text{ cm}^{-1}$) and OH stretching ($3600\text{ to }3720\text{ cm}^{-1}$) ranges. The
636 characteristic bands of antigorite ($373, 1043, 3670\text{ and }3700\text{ cm}^{-1}$) and lizardite ($390, 3680,$
637 3703 cm^{-1}) are indicated in grey. (a) Raman spectra of lizardite and chrysotile. (b) Raman
638 spectra of antigorite related to the T_{\max} . (c) Raman spectra of mixed lizardite/antigorite
639 serpentine.

640

641 Fig. 4. Photomicrographs of characteristic textures of serpentinite from the study area: Atg,
642 antigorite; lz, lizardite; Chr, chrysotile; Mag, magnetite; x, polarized light; x', crossed-
643 polarized light. The T_{\max} obtained from the associated metasediments is also indicated.

644 (a-a'). Sample ICH2 (Chenaillet massif). Mesh texture developed from olivine is observed in
645 locations where lizardite is the only developed serpentine species. At the top of the image,
646 secondary veins infilled by chrysotile cross-cut the mesh texture.

647 (b-b'). Sample CR02 comes from the low-temperature blueschist domain (Cristillan massif).
648 The sample is dominated by mesh texture underlined by lizardite. Secondary antigorite
649 crystallized at the boundary of the lizardite minerals. In the antigorite zone, relics of lizardite
650 (brownish minerals) are still present.

651 (c-c'). Sample RQ23 comes from medium-temperature blueschist domain (Rocca Bianca
652 massif). The sample is equally dominated by lizardite and antigorite. In the lizardite-dominant
653 zone (greenish color), the mesh texture is partly preserved; however, antigorite developed at
654 the expense of lizardite at the grain boundaries. Antigorite minerals with interlocked
655 microstructures also form millimeter-sized patches that are free of lizardite relics.

656 (d-d'). Sample RQ16 comes from the intermediate-temperature blueschist domain (Refuge du
657 Viso). The sample is dominated by antigorite minerals, which are developed in a dense
658 network of veins at the expense of lizardite preserved in mesh texture.

659

660 Fig. 5. Photomicrographs of characteristic textures of serpentine species from the western
661 Alps: Atg, antigorite; Lz, lizardite; Chr, chrysotile; Mag, magnetite; x, polarized light; x',
662 crossed-polarized light. The T_{\max} obtain on the associated metasediments is also indicated.

663 (a-a'). Sample BB01 comes from the high-temperature blueschist domain (Bric Bouchet
664 massif). This sample is dominated by antigorite. The magnetite underlines the early mesh
665 structure.

666 (b-b'). Sample RQ01 comes from the high-temperature blueschist domain (Traversette
667 massif). In this sample, only antigorite is observed. Mesh and bastite textures are well
668 preserved, suggesting a static crystallization of antigorite, most likely at the expense of early
669 lizardite produced during ocean floor metamorphism.

670 (c-c'). Sample Vi01 comes from Monviso eclogitic ophiolite. The antigorite is the only
671 serpentinite species that preserves the mesh texture underlined by magnetite.

672

673 Fig. 6. Microprobe analyses (in weight %) of serpentinite samples plotted in an Al_2O_3 versus
674 SiO_2 diagram (cf Table 3). The arrow indicates the metamorphic trend from sub-greenschist
675 to eclogitic metamorphic facies conditions. The antigoritization processes in the serpentinites
676 are characterized by a chemical homogenization associated with the increase in the
677 metamorphic conditions.

678

679 Fig. 7. Idealized sketch determined from natural serpentinites that shows the evolution of the
680 antigoritization processes under a HP metamorphic gradient. (a) Characteristic Raman spectra
681 of serpentine species from the study area. The bands of antigorite (373, 1043, 3670 and 3700
682 cm^{-1}) are indicated in grey. (b) In sub-greenschist conditions, only lizardite is present. (c) In
683 LT-blueschist, antigorite appears along the lizardite grain boundaries via a dissolution-
684 precipitation process. (d) In MT-blueschist, the antigorite becomes the major phase. The veins
685 of antigorite at the lizardite grain boundaries widen and the cores of lizardite show a mixed
686 lizardite/ antigorite Raman spectra related to the onset of the solid-state transition. (e) In HT-
687 blueschist, antigorite becomes the sole serpentine variety. Antigorite develops infra-
688 millimetric blades superimposed over the original mesh texture.

689

690 Fig. 8. Phase diagram of antigorite and lizardite (after Evans, 2004): Lz, lizardite; Atg,
691 antigorite; Chr, chrysotile; Fo, forsterite; Tlc, talc; Brc, brucite. Reactions (1) and (3)
692 correspond to the onset of the reactions while (1') and (3') correspond to the end of these

693 reactions with the complete consumption of lizardite. Metamorphic facies are from Spear
694 (1993). The natural stability field domain of coexisting lizardite and antigorite is restricted to
695 a temperature range between ~320 and 390°C. At 390°C and above, the lizardite is entirely
696 replaced by antigorite. Above 460°C, Reaction (4) results in the onset of crystallization of
697 olivine. Between 320 and 390°C, the antigorite develops though Reaction (3) in the presence
698 of SiO₂-rich fluids by dissolution-precipitation processes. Between 340 and 380°C, Reaction
699 (2) is also observed in the core of lizardite antigorite by solid-state transformation.

700

701 Table 1. RSCM results with longitude (Long.) and latitude (Lat.) in decimal degrees
702 (WGS84), number of Raman spectra (n), R2 ratio (mean and standard deviation) and T_{max}
703 (mean and 1-σ uncertainty).

704

705 Table 2. Mineral assemblage of the studied serpentinites as detected by XRD, with (+ + +)
706 major phase, (+) minor phase (<10%), and (-) absent or below detection limit (<1%). Facies
707 metamorphic conditions and T_{max} are also given. The black star indicates the presence of
708 antigorite.

709

710 Table 3. Representative microprobe analyses of serpentine minerals from alpine serpentinites.
711 All values are in wt% (b.d.l. = below detection limit; n.d. = not determined).